

## Observation of contact angle hysteresis due to inhomogeneous electric fields

Wei Wang<sup>1,2,3</sup>, Qi Wang<sup>1,3</sup>, Jia Zhou<sup>1</sup>✉ & Antoine Riaud<sup>1</sup> ✉

Static contact angle hysteresis determines droplet stickiness on surfaces, and is widely attributed to surface roughness and chemical contamination. In the latter case, chemical defects create free-energy barriers that prevent the contact line motion. Electrowetting studies have demonstrated the similar ability of electric fields to alter the surface free-energy landscape. Yet, the increase of apparent static contact angle hysteresis by electric fields remains unseen. Here, we report the observation of electrowetting hysteresis on micro-striped electrodes. Unlike most experiments with stripes, the droplet spreading on the substrate is experimentally found to be isotropic, which allows deriving a simple theoretical model of the contact angle hysteresis depending the applied voltage. This electrowetting hysteresis enables the continuous and dynamic control of contact angle hysteresis, not only for fundamental studies but also to manufacture sticky-on-demand surfaces for sample collection.

<sup>1</sup>State Key Laboratory of ASIC and System, School of Microelectronics, Fudan University, Shanghai, China. <sup>2</sup>MOE Key Laboratory of Material Physics and Chemistry under Extraordinary Conditions, School of Physical Science and Technology, Northwestern Polytechnical University, Xi'an, China. <sup>3</sup>These authors contributed equally: Wei Wang, Qi Wang. ✉email: [jia.zhou@fudan.edu.cn](mailto:jia.zhou@fudan.edu.cn); [antoine\\_riaud@fudan.edu.cn](mailto:antoine_riaud@fudan.edu.cn)

On most surfaces, the liquid–solid contact angle  $\theta$  can adopt a range of values before the contact line starts moving<sup>1–3</sup>. This static contact angle hysteresis (CAH; the difference between the advancing and receding contact angles) is mainly attributed to surface roughness<sup>4,5</sup> and chemical heterogeneities<sup>6,7</sup>. Despite its major implications in determining the adhesion of paint to surfaces and pesticides to leaves<sup>2</sup>, CAH remains highly challenging to study experimentally because it is a macroscopic phenomenon excessively sensitive to nanometer-scale defects. Hence, experimental surfaces need to be prepared with the greatest care and quantitative well-controlled experiments are scarce<sup>7,8</sup>. In most cases, patches of a selected contaminant (such as octadecanethiol<sup>9</sup>) are carefully deposited on an ultra-clean polished surface to form surface-adsorbed monolayers of well-controlled composition. There is a widespread consensus that these patches of contaminant create free-energy barriers that prevent the contact line motion<sup>1,10</sup>. This modification of the free-energy landscape is well described by the Gibbs isotherm  $\frac{\partial \gamma_0}{\partial \mu_i} = -\Gamma_i$ , with  $\Gamma_i$  the surface coverage of a contaminant  $i$ ,  $\mu_i$  its chemical potential, and  $\gamma_0$  the local surface tension. Hence, once the composition of the surface is set, the surface energy landscape is not allowed to vary anymore, which makes CAH experiments extremely work-intensive.

Over the past two decades, electrowetting has emerged as a convenient way to control the apparent contact angle of liquid droplets by adjusting the effective liquid–solid interfacial tension using electric fields<sup>11–20</sup>. While electrowetting was originally explained by Lippmann on thermodynamic grounds<sup>21</sup>, Jones<sup>22</sup> and Buehrle et al.<sup>23</sup> have clarified that the liquid–solid interfacial tension and the contact angle are not affected by the electric fields<sup>24</sup> but that the interface profile is gradually evolving from the intrinsic Young–Dupré contact angle to the apparent Young–Lippmann contact angle<sup>25</sup>. The length of this transition depends on the electrowetting set-up but is generally negligible compared to the droplet size as it most often occurs within 1  $\mu\text{m}$  from the contact line.

Outside this transition region, the thermodynamic identity derived by Lippmann is recovered by posing the effective interfacial tension  $\gamma = \frac{\partial F}{\partial A}$  as the generalized free energy per unit solid–liquid surface area  $A$ <sup>26</sup>. The generalized free-energy  $F = E - Q\Phi - \sum_i \mu_i n_i$  offsets the Helmholtz free-energy  $E$  so that it is minimized at thermodynamic equilibrium under fixed electric potential  $\Phi$  and chemical potential, regardless of the amount  $n_i$  of species  $i$  and of the electric charge  $Q$ . Using Maxwell identities on  $F$  yields the celebrated Lippmann equation (additional discussion and derivation available in Supplementary Note 1):

$$\frac{\partial \gamma}{\partial \Phi} = -\sigma, \quad (1)$$

with  $\sigma$  the areal surface charge. We note the striking analogy between Eq. (1) and the Gibbs isotherm with the variables:

$$\gamma_0 \leftrightarrow \gamma, \mu_i \leftrightarrow \Phi, \Gamma_i \leftrightarrow \sigma. \quad (2)$$

This analogy suggests that surface charges and electric fields may also influence the CAH on a scale larger than the electrowetting transition region. Such electrical control of CAH may open exciting strategies for liquid collection and release by reversibly switching the surface between sticky and non-sticky states, respectively. More broadly, it might enable quantitative CAH studies that (i) do not rely on immutable defects and (ii) investigate a continuous range of advancing and receding conditions. This electrically induced CAH has recently been used in a series of elegant experiments to create dynamic pinning sites and guiding rails for sliding drops<sup>27,28</sup>, but never been studied for its own, in terms of advancing and receding contact angles. Besides those studies, most experiments in electrowetting phenomena

report either no effect<sup>29–31</sup> or even a reduction<sup>32,33</sup> of CAH due to the application of an electric voltage.

This confusing disagreement between the thermodynamic analogy and experimental evidences is mainly due to three reasons. First, instead of the static CAH<sup>1–3</sup> observed at mechanical equilibrium, most electrowetting studies are concerned with moving droplets and therefore focus on the more complex dynamic CAH, which involves viscous and inertial forces that may affect the hysteresis<sup>29</sup>. For instance, Nelson et al.<sup>29</sup> did not report any increase in CAH when the droplet speed  $v$  (measured in terms of capillary number  $\text{Ca} = \frac{\mu v}{\gamma}$ , with  $\mu$  the dynamic viscosity of the liquid) was small ( $\text{Ca} < 10^{-4}$ ). Second, by analogy with chemical heterogeneities and surface roughness, the electrical control of CAH should require inhomogeneous (that is, spatially varying) electric fields, which were used only in a handful of reports<sup>30,34</sup>. We note that homogeneous electric fields can increase the droplet friction by expanding the three-phase contact perimeter<sup>35</sup> or may also alter the CAH by triggering a wetting state transition<sup>36</sup>, but the CAH in each state is then controlled by the surface roughness and not by the electric field. Similarly, droplets immersed in an oil phase could exhibit CAH due to the thinning of the oil layer underneath the droplet as the voltage is increased<sup>37</sup>, but this phenomenon has no analog to CAH in air. Third, the definition of hysteresis differs between electrowetting conventions and the usual wetting phenomena due to chemical heterogeneities and surface roughness. Indeed, the CAH is obtained by recording the onset of contact line motion, which can be achieved in two ways in electrowetting studies: (i) by hydrostatic stress without changing the surface energy landscape (such as inclining the plane or pumping the liquid) or (ii) by ramping up the actuation voltage to change the surface energy landscape<sup>2,30,34</sup>. In the latter case, Zhao et al.<sup>38</sup> attributed the CAH to a combination of wetting defects of constant energy, contact line friction, and volumetric shear in the droplet, which are the same forces as for the dynamic CAH, which does not allow to conclude on the ability of electric fields to modify the static CAH. In summary, to observe a variation of static CAH due to electric fields analog to the CAH induced by chemical defects, the following conditions should be met: (i) the contact line must move without changing the surface free energy landscape, (ii) direct current (DC) voltage should be used instead of alternating current, (iii) the electric field must be heterogeneous. So far, except for refs. 27,28 (which did not study on CAH but only contact line pinning), these conditions have not been fulfilled.

Here we demonstrate the direct analogy of static CAH by applying an inhomogeneous electric field while pumping liquid in the droplet. A thermodynamic model is derived to describe the evolution of advancing and receding apparent contact angles. Similarly to earlier works on CAH<sup>6,10,39</sup>, our model overlooks the finest details of the contact line structure such as the precursor wetting film<sup>40</sup>, Van der Waals force<sup>41</sup>, and Lorentz force acting at the interface<sup>23</sup>. Despite these simplifications, it captures well the key features of the experimental observations, including a quadratic dependence on the actuation voltage and an unexpected influence of the droplet contact line radius.

## Results and discussion

**Experimental increase of the apparent CAH with electrical voltage.** The experimental set-up<sup>42</sup>, shown in Fig. 1a–c, is similar to the dielectrowetting chip used previously by McHale et al.<sup>30</sup>. A periodic array of indium tin oxide (ITO) interdigitated electrodes (IDEs, 50  $\mu\text{m}$  finger width and spacing, 130 nm thick) ensures the generation of an inhomogeneous electric field, which is fundamental to observe a CAH. This field is reminiscent of the stripes used in several studies of CAH (see ref. 43 and references therein). A dielectric cyanoethyl pullulan (CEP) layer (408 nm thick) insulates the liquid from the electrodes<sup>44</sup> so that the whole droplet behaves like an ideal conductor (dielectric relaxation time  $\tau_e = \epsilon_1/\sigma_1 \simeq 1.3 \times 10^{-4}$  s,

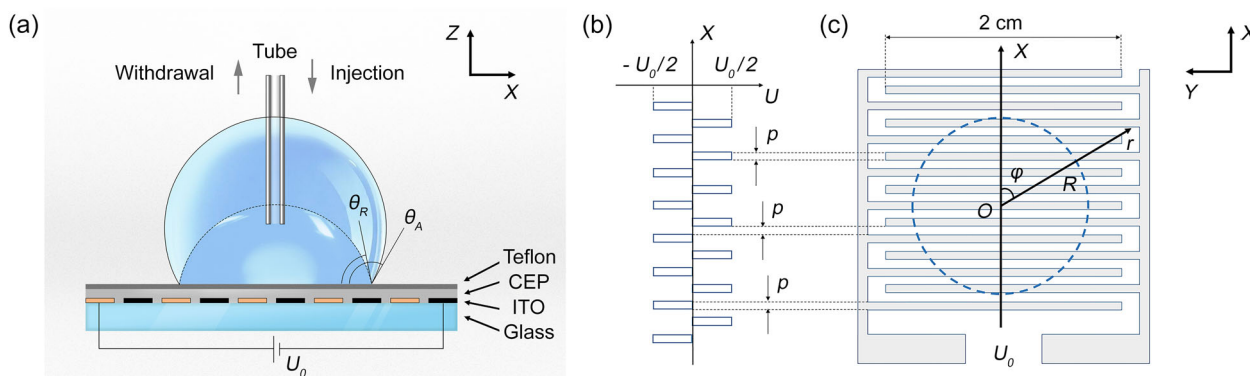


**Fig. 1 Experimental set-up.** **a** Side view. The liquid is replenished or extracted via a steel tubing. The indium tin oxide (ITO) interdigitated electrodes (IDE) are isolated from the liquid by a dielectric layer of cyanoethyl pullulan (CEP) and a hydrophobic layer of Teflon and connected to a DC supply of voltage  $U_0$ . Side view images were captured and analyzed using a goniometer. The two droplet profiles illustrate the droplet shape when the contact line is unpinning as the contact angle escapes  $[\theta_R, \theta_A]$  range, with  $\theta_R$  and  $\theta_A$  the receding and advancing contact angles, respectively. **b** Voltage across the solid-liquid interface in  $x$  direction. Due to the large aspect ratio of the IDEs, the electric potential is well approximated by a square-wave function<sup>61,62</sup> with  $p$  being the finger width and spacing of the electrodes. **c** Top view. The gray drawing is a representation of the interdigitated electrodes. The contact line radius of the droplet is denoted by  $R$ . In these polar coordinates, the origin  $O$  is located at the center of the circular contact area (dashed circle), with  $\varphi$  and  $r$  the angular and radial coordinates, respectively.

with  $\epsilon_1 \simeq 80\epsilon_0$  and  $\epsilon_0 = 8.85 \times 10^{-12}$  F/m the dielectric permittivity of water and vacuum, respectively, and  $\sigma_1 \leq 5.6 \times 10^{-6}$  S/m the conductivity of deionized (DI) water). Since electrowetting can only reduce the contact angle, a thin hydrophobic polytetrafluoroethylene (PTFE) layer (60 nm thick) is coated on the dielectric layer to maximize the operating range. Even though triboelectric and electrically controlled charging of PTFE in contact with water have been reported<sup>45–47</sup>, we neglect these effects on the CAH here. Indeed, Li and Mugele did not report any increase in CAH<sup>32</sup> when using a similar set-up but with a uniform electrode. A steel tubing is used to replenish or extract liquid during CAH measurements. The tubing is not electrically connected.

For a given voltage, a 40  $\mu\text{L}$  DI water droplet is deposited on the chip and spreads by electrowetting until it reaches a stable shape. Then, the droplet volume is slowly varied by pumping liquid via the tubing. The relatively low flow rate  $Q_1 = 1.0 \mu\text{L}/\text{min}$  ensures (i) that the droplet behaves as an ideal conductor (the characteristic pumping time  $\tau_p = V_1/Q_1 \simeq 40 \text{ min} \gg \tau_e$  with  $V_1$  the droplet volume) and (ii) that the droplet shape is always near mechanical equilibrium ( $\tau_{\text{cap}} = \sqrt{\frac{\rho_1 V_1}{\gamma_{\text{lg}}}} \simeq 23 \text{ ms} \ll \tau_p$  with  $\tau_{\text{cap}}$  the mechanical relaxation time,  $\rho_1 \simeq 1000 \text{ kg}/\text{m}^3$  and  $\gamma_{\text{lg}} \simeq 71.97 \text{ mN}/\text{m}$  the density and surface tension of water in air) and dynamic CAH can be neglected. Due to the CAH, the contact line remains trapped during the pumping cycles until the deformation overcomes the static CAH. Hence, although the volume may vary by tens of microliters, advancing and receding contact line radii remain the same for a constant voltage through the entire experiment. Side view images of the droplet are captured to measure contact angles with a goniometer (DSA30, KRÜSS, Germany). After each acquisition, the surface is cleaned, and the experiment is repeated with a different voltage.

The measured apparent contact angles for  $U_0$  ranging from  $-100$  to  $+100 \text{ V}_{\text{DC}}$  in the directions parallel and orthogonal to the electrodes are reported in Fig. 2a, b. In agreement with the Lippmann–Young equation and other electrowetting experiments<sup>12,14,48</sup>, the contact angle decreases with the voltage until  $|U_0|$  reaches approximately  $50 \text{ V}_{\text{DC}}$ , above which electrowetting saturation occurs. Given the controversy surrounding the origins of electrowetting saturation<sup>49–53</sup>, we restrict this study to the low-voltage region ( $|U_0| < 50 \text{ V}_{\text{DC}}$ ).

**Isotropic droplet spreading.** It is widely reported that droplets become elongated as they spread on stripes, where the stripes can be

not only microgrooves<sup>4</sup> and chemical defects<sup>9,54,55</sup> but also electrodes<sup>30</sup>. However, we observe that the droplet CAH (measured as the difference between advancing and receding contact angles) and its contact radius remain isotropic as long as the voltage remains below the saturation voltage (see Fig. 2c, d, side view of the droplets are shown in Supplementary Movie 1 and additional pictures of the droplet at various voltages, droplet aspect ratio compared to theory<sup>54</sup>, and droplet contact line photographs are available in Supplementary Note 6 Figs. S10–S12, respectively). While we have no definite explanation for this phenomenon, we note that such nearly isotropic spread has been previously reported for chemical nanostripes<sup>56</sup>, and one can also check that the slight anisotropy observed by Banpurkar et al.<sup>57</sup> is considerably lower than its theoretical value based on the model for chemical stripes<sup>54,55</sup>. These observations fit a pattern where the droplet spreading becomes more isotropic when the stripes scale similarly with the detailed contact line structure. In the case of chemical defects, the contact line fine structure evolves over tens of nanometers<sup>58</sup>, therefore only nanostripes would yield an isotropic spreading<sup>56</sup>, whereas the contact line in electrowetting evolves over a micrometric scale<sup>59</sup>, so that even microstripes could drive an isotropic spreading. Checking the origin of this effect would require considerable effort and is out of the scope of the current work; hence, for the time being, we will assume the droplet to remain circular with an isotropic apparent contact angle.

**Effect of electrode pitch on CAH.** Similar experiments were repeated with initial droplet volumes ranging from 10 to 40  $\mu\text{L}$  with a  $p = 50 \mu\text{m}$  electrode pitch. For each case, the difference between advancing and receding contact angles (shown in Fig. 2a, b for 40  $\mu\text{L}$  droplets) yield the apparent static CAH shown in Fig. 3a–d. Unlike other studies<sup>29–33</sup> (see Supplementary Note 8), we observe an increase of apparent CAH as  $|U_0|$  increases from 0 to  $50 \text{ V}_{\text{DC}}$ . We note that the CAH increase of the smallest droplets (10  $\mu\text{L}$ ) is almost twice that of the largest ones ( $8.0^\circ$  compared to  $4.4^\circ$ ). This size dependence of the apparent CAH hints at the importance of the spatial scale of the electric field.

In order to vary the spatial scale of the electric field, we increased the electrode pitch. For the sake of clarity, we only show 0 and 40 V in Fig. 4, while varying the initial droplet volumes from 10 to 50  $\mu\text{L}$  and the electrode pitch from 50 to 200  $\mu\text{m}$  (comparison over a broader range of voltages is available in Fig. S7 in Supplementary Note 5). These experiments were carried out immediately after manufacturing the substrates, resulting in a very low CAH ( $3.1^\circ$ ) in

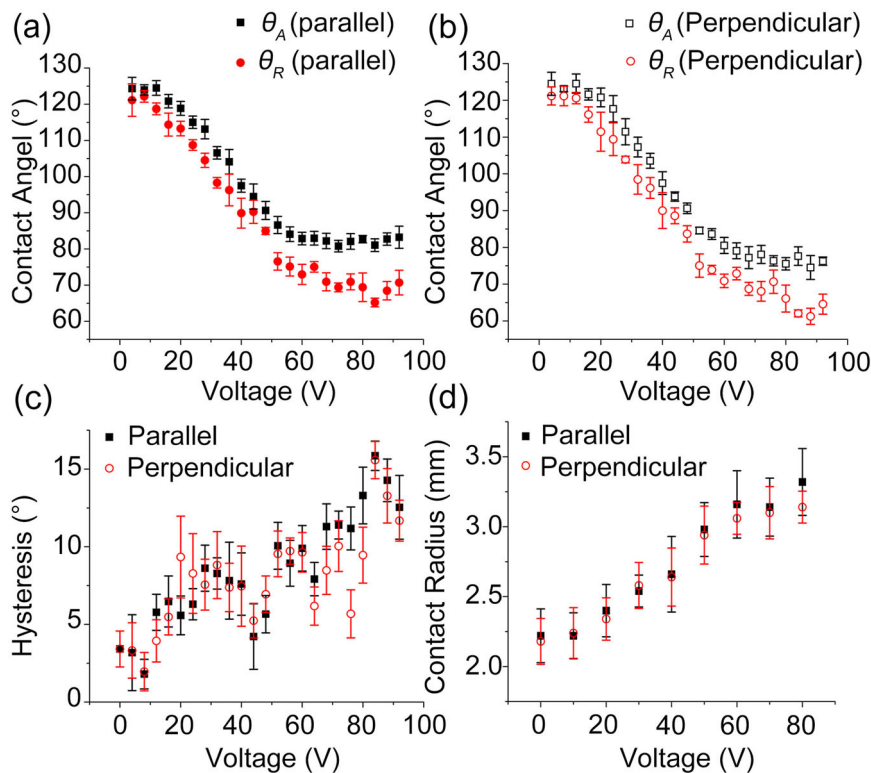


**Fig. 2** Effect of the electric voltage on apparent contact angles of 40  $\mu\text{L}$  droplets. **a** Advancing and receding contact angle parallel to the electrodes. **b** Advancing and receding contact angle perpendicular to the electrodes. **c** Contact angle hysteresis in parallel and perpendicular directions. **d** Spreading radius in parallel and perpendicular directions. Experimental data are averaged over five independent measurements, the error bars indicate the standard error.

the absence of electric voltage. Regardless of the electrode pitch, the apparent CAH under 40 V is 3–6 times larger than the intrinsic CAH. The growth of CAH with the electrode pitch confirms that electric field inhomogeneity are a key ingredient of the apparent CAH. Furthermore, we observe that all the experimental data points at a given voltage  $U_0$  collapse in a single line when rescaling the droplet radius  $R$  with the electrode pitch  $p$  as  $p/R$ .

**Thermodynamic interpretation of the apparent CAH.** In the following, we model the static CAH below saturation regime as a function of the actuation voltage within the framework developed by Johnson and Dettre<sup>6</sup>. The apparent contact angle is obtained by finding the apparent contact line radius  $R$  that minimizes the generalized free energy  $F = F_{sl} + F_{lg} + F_{sg}$  of the system, with  $F_{sl}$ ,  $F_{lg}$ , and  $F_{sg}$  the generalized free energies of the solid–liquid, liquid–gas, and solid–gas interfaces, respectively. The elementary displacement  $\partial R$  is taken much smaller than the IDE width<sup>43</sup> but much larger than the transition region (approximately the combined thickness of the hydrophobic and dielectric layers, that is 0.5  $\mu\text{m}$ ) so that variations of generalized free energy at the contact line are negligible compared to the variations of solid–liquid free energy. Assuming that the droplet remains circular at all times and that the contact angle is isotropic, which was verified for two orthogonal directions (Fig. 2c, d), geometrical construction yields  $\partial F_{lg}/\partial R = 2\pi R\gamma_{lg}\cos\theta$  and  $\partial F_{sg}/\partial R = -2\pi R\gamma_{sg}$ , with  $\gamma_{lg}$  and  $\gamma_{sg}$  the liquid–gas and solid–gas interfacial tensions, respectively<sup>60</sup>. The derivation of  $\partial F_{sl}/\partial R$ , which differs from the classical Young–Dupré equation<sup>60</sup>, is our main concern.

By definition,  $F_{sl} = \epsilon_{CL} + C + \int_0^R \int_{-\pi}^{\pi} \gamma_{sl} r dr d\varphi$  with  $\epsilon_{CL}$  the free energy in the transition region,  $C$  a constant,  $\gamma_{sl}$  the solid–liquid effective interfacial tension, and  $\varphi$  and  $r$  the angular and radial coordinates, respectively (see Fig. 1). Because the transition region is

much smaller than the elementary volume that we are studying,  $\epsilon_{CL}$  is much smaller than  $F_{sl}$ . Elementary calculus yields:

$$\frac{\partial F_{sl}}{\partial R} = R \int_{-\pi}^{\pi} \gamma_{sl} d\varphi. \quad (3)$$

The integral operator in Eq. (3) averages the variations of energy due to each stripe over the entire droplet surface, such that local energy barriers are smoothed into small global energy humps. Thus, large droplets encompassing many stripes will experience a smaller relative variation of free energy than smaller ones as they cross a stripe.

We evaluate  $\gamma_{sl}$  by assuming that the electric field varies continuously at the microscale and can thus be locally integrated from Eq. (1):

$$\gamma_{sl} = [\gamma_{sl_0}] - \frac{C}{2} U^2, \quad (4)$$

with  $U$  and  $C$  the effective voltage across the solid–liquid interface and the areal capacitance between the electrodes and the liquid (this parameter is determined experimentally in Fig. S2 in Supplementary Note 2).  $[\gamma_{sl_0}]$  is the intrinsic interfacial tension, that is,  $\gamma_{sl}$  in the absence of electric field. The  $[\ ]$  notation indicates that, due to chemical impurities<sup>1</sup>,  $[\gamma_{sl_0}]$  is susceptible to vary between a lower and upper bound given by  $[\gamma_{sl_0}]$  and  $[\gamma_{sl_0}]$ , respectively. According to Young–Dupré equation<sup>2</sup>, the advancing contact angle  $\theta_{A0}$  and receding contact angle  $\theta_{R0}$  at zero voltage satisfy  $\cos\theta_{A0} = (\gamma_{sg} - [\gamma_{sl_0}])/\gamma_{lg}$  and  $\cos\theta_{R0} = (\gamma_{sg} - [\gamma_{sl_0}])/\gamma_{lg}$ , respectively.

For a regular array of IDEs as shown in Fig. 1b, the effective voltage  $U$  is half of the externally applied voltage  $U_0$  (see Supplementary Note 3 for the full derivation):

$$U^2 = \left(\frac{U_0}{2}\right)^2 \Pi(kx), \quad (5)$$

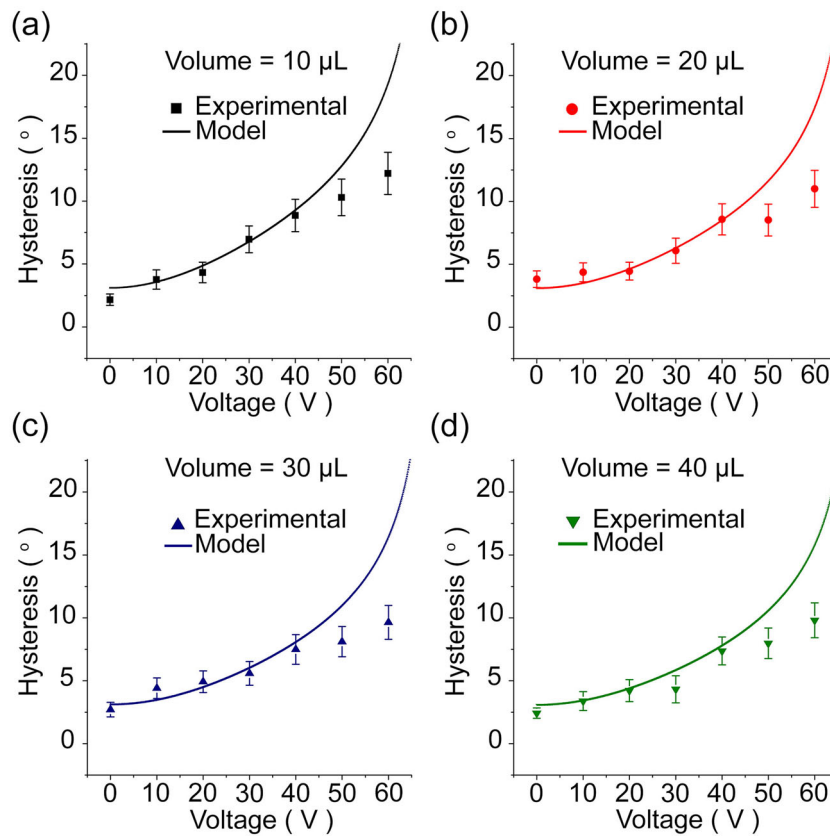


**Fig. 3 Voltage-dependent hysteresis for different initial droplet volumes.** The initial droplet volumes are **a** 10 μL, **b** 20 μL, **c** 30 μL, and **d** 40 μL, respectively. The pitch width of the interdigitated electrodes is 50 μm. The solid lines were obtained based on our model (Eq. (10)) with contact radii calculated using the Young-Laplace equation (see Supplementary Note 4). Each experimental dot was averaged over 16 independent measurements and the error bars indicate the standard error. Note that the model is only relevant for voltages below contact angle saturation ( $\lesssim 50$  V).

where  $\Pi$  is the square-wave function denoting the distribution of the electric potential energy (1 above the electrodes and 0 elsewhere, similar to the hysteresis-prone mesa-type landscape of Joanny and De Gennes<sup>39</sup>), and  $k$  denotes the wavenumber  $\pi/p$  with  $p$  the finger width and also the spacing (see Fig. 1)<sup>61,62</sup>. Integration of Eq. (3) is simpler when  $\Pi$  is expressed as a Fourier series:

$$\Pi = \frac{1}{2} + \sum_{n=0}^{\infty} \frac{2(-1)^n}{(2n+1)\pi} \cos[(2n+1)kr \cos \varphi]. \quad (6)$$

Substituting Eqs. (4)–(6) in Eq. (3) and using the identity  $\int_{-\pi}^{\pi} \cos(\tau \cos \varphi) d\varphi = 2\pi J_0(\tau)$  with  $J_0$  the 0-order Bessel function, we get:

$$\frac{\partial F_{sl}}{\partial R} = 2\pi R \left\{ [\gamma_{sl_0}] - \gamma_L - \gamma_H \right\}, \quad (7a)$$

$$\gamma_L = \frac{CU_0^2}{16}, \quad (7b)$$

$$\gamma_H = \frac{CU_0^2}{8} \sum_{n=0}^{\infty} \frac{2(-1)^n}{(2n+1)\pi} J_0[(2n+1)kR]. \quad (7c)$$

It contains three terms: the intrinsic interfacial tension  $[\gamma_{sl_0}]$ , the average decrease in effective interfacial tension  $\gamma_L$  (see ref.<sup>34</sup> for IDEs), and an oscillating term  $\gamma_H$  that results in an effective hysteresis effect but did not appear in previous studies. For uniform potential distributions ( $k \rightarrow 0$ ), Eq. (7a) reduces to the standard Lippmann–Young equation. In the current experiments,  $R \gg p$ , so  $J_0(\tau) \simeq \sqrt{\frac{2}{\pi\tau}} \cos(\tau - \frac{\pi}{4})$ , which simplifies Eq. (7c) to

$$\gamma_H \approx \frac{CU_0^2}{8\sqrt{\pi k R}} \sum_{n=0}^{\infty} \frac{2\sqrt{2}(-1)^n}{\pi(2n+1)^{3/2}} \cos \left[ (2n+1)kR - \frac{\pi}{4} \right]. \quad (8)$$

In the Supplementary Note 3, we postulate that the upper and lower bounds of  $\gamma_H$  read:

$$-B \frac{CU_0^2}{16} \sqrt{\frac{p}{R}} < \gamma_H < B \frac{CU_0^2}{16} \sqrt{\frac{p}{R}}, \quad (9)$$

with  $B = \frac{4-\sqrt{2}}{\pi^2} \zeta(\frac{3}{2}) \approx 0.684$  and  $\zeta$  the Riemann zeta function. Interestingly, Eq. (9) indicates the dependence of static CAH on  $\sqrt{\frac{p}{R}}$ .

Finally, substituting Eq. (9) in Eq. (7a) and minimizing the generalized free energy  $F$  yields:

$$\cos \theta_A < \cos \theta < \cos \theta_R \quad (10a)$$

$$\cos \theta_A = \cos \theta_{A0} + \frac{CU_0^2}{16\gamma_{lg}} - B \frac{CU_0^2}{16\gamma_{lg}} \sqrt{\frac{p}{R}} \quad (10b)$$

$$\cos \theta_R = \cos \theta_{R0} + \frac{CU_0^2}{16\gamma_{lg}} + B \frac{CU_0^2}{16\gamma_{lg}} \sqrt{\frac{p}{R}} \quad (10c)$$

The upper and lower bounds of the contact angle in Eq. (10a) correspond to the receding apparent contact angle  $\theta_R$  and the advancing apparent contact angle  $\theta_A$ , respectively.

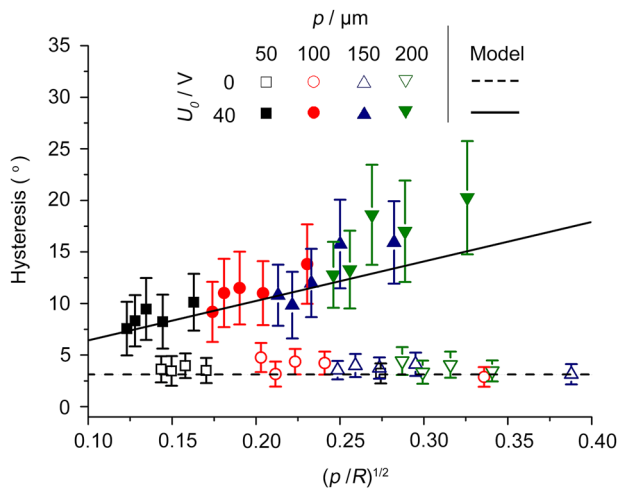


**Fig. 4 Analytical prediction of the contact angle hysteresis over a range of initial droplet volumes and electrode pitch.** The contact angle hysteresis is measured at voltage  $U_0$  0 and 40 V with electrode pitches  $p$  ranging from 50 to 200  $\mu\text{m}$  and initial droplet volumes of 10, 20, 30, 40, and 50  $\mu\text{L}$ . The symbols indicate the electrode pitch while increasing contact line radii  $R$  with identical symbols reflect increasing droplet volumes. For experimental and theoretical data points,  $R$  was estimated by solving the Young-Laplace equation. Each experimental dot (hysteresis angle) was averaged over five independent measurements and the error bars indicate the standard error. The theoretical contact angle hysteresis is obtained by subtracting advancing and receding contact angles from Eq. (10b). In the model, the surface tension of water in air is  $\gamma_{\text{lg}} = 71.97$  mN/m, and the fitting parameters are the advancing contact angle at zero voltage  $\theta_{A0} = 123.8^\circ$ , the receding contact angle at zero voltage  $\theta_{R0} = 120.7^\circ$ , and the effective areal capacitance (see Supplementary Note 2)  $C = 0.350$  mF/m $^2$ .

Subtracting Eq. (10b) from Eq. (10c) yields Eq. (11a), then assuming that the CAH remains small yields Eqs. (11b) and (11c):

$$\delta \cos \theta_R - \delta \cos \theta_A = B \frac{CU_0^2}{8\gamma_{\text{lg}}} \sqrt{\frac{p}{R}} \quad (11a)$$

$$\theta_A - \theta_R = \frac{[\gamma_{\text{sl}_0}] - [\gamma_{\text{sl}_0}]}{\gamma_{\text{lg}} \sin \theta_E} + \frac{BCU_0^2}{8\gamma_{\text{lg}} \sin \theta_E} \sqrt{\frac{p}{R}} \quad (11b)$$

$$\cos(\theta_E) = \cos(\theta_{E0}) + \frac{CU_0^2}{16\gamma_{\text{lg}}} \quad (11c)$$

with  $\delta \cos \theta_i = \cos \theta_i - \cos \theta_{i0}$  for  $i = R$  or  $A$  and  $\theta_E = (\theta_A + \theta_R)/2$ . According to these expressions, the CAH does not depend directly on the droplet volume but instead is set by the contact line radius, which depends only on the initial droplet volume. Equation (11a) provides an energetic viewpoint that singles out the electrical effect on the effective CAH, while Eq. (11b) is a convenient expression for experimental purposes. The first term in Eq. (11b) describes the hysteresis due to surface defects, while the second represents the electrowetting hysteresis. We note that  $1/\sin(\theta_E)$  is a decreasing function of the actuation voltage on the studied interval (0–40 V) and therefore cannot be responsible for the observed increase in CAH (the contribution of both terms is shown in Supplementary Note 5 Fig. S6). This suggests that non-electric field defects will have a decreasing influence on the apparent CAH as the contact angle decreases. This is consistent with the observations of Li and Mugele<sup>32</sup> who observed a decrease in CAH for increasing voltages (on uniform electrodes) and with total wetting experiments where contact line pinning is seldom observed regardless of the surface state.

**Model validation.** Equations (10b) and (10c) predict the CAH depending on the actuation voltage, electrode pitch, and droplet radius. Other parameters are obtained once for the whole set of experiments, as described in “Methods.” We used  $\gamma_{\text{lg}} = 71.97$  mN/m (for DI water),  $\cos \theta_{A0} = -0.556$ ,  $\cos \theta_{R0} = -0.510$ , and  $C = 0.350$  mF/m $^2$ .

The predictions of Eqs. (10b) and (10c) are compared to experimental results for a range of initial droplet volumes and actuation voltages in Fig. 3, showing good agreement with the parabolic behavior predicted by our model for voltages below the electrowetting saturation. The larger apparent CAH of small droplets is also well accounted for. Furthermore, our model also performed well when replacing CEP in the dielectric layer by SU8-2002 (see Supplementary Note 7).

An equally good agreement is obtained over a range of electrode pitches and initial droplet volume in Fig. 4. Consistently with Eq. (11b), the apparent CAH scales as  $\sqrt{p/R}$  for all the initial droplet volumes and electrode pitches. Although this scaling may seem at odds with well-established theories of CAH based on the Cassie–Baxter framework<sup>43</sup>, it is a direct consequence of the assumption of isotropic droplet spreading. When the stripes are wide enough<sup>56</sup>, the droplet contact line should become trapped over the electrodes<sup>30,43</sup> and begin to elongate. Using fractal electrodes or electrodes with a broad range of feature sizes would likely yield a more size-independent contact angle hysteresis. The solid line in Fig. 4 shows the model prediction at 40 V and confirms the slope  $\frac{BCU_0^2}{8\gamma_{\text{lg}} \sin \theta_E}$ . The model begins to underestimate the experimental data at large electrode pitch ( $\sqrt{p/R} \simeq 0.25$ ), after which the droplet starts to lose its circular shape<sup>30,63</sup> (contact radii observed in two directions are shown in Figs. S8 and S9 in Supplementary Note 6).

## Conclusions

In summary, we report the experimental control of static apparent CAH by an inhomogeneous electric field, in formal analogy with chemical defects. Noting that the droplet spreads in an isotropic fashion, we derive a thermodynamic model to interpret these observations for small CAH. At this isotropic spreading regime, our model predicts that the CAH depends on the electrode (defect) pitch, which differs from usual CAH studies involving stronger defects. It is also inferred that the CAH grows quadratically with the actuation voltage. These predictions are confirmed against experimental data, even though the model slightly underestimates the experimental hysteresis at large electrode pitch. This study offers a controlled and dynamic setting to clarify the role of CAH on the adhesion of liquids and biofluids to surfaces and also provides a feasible approach for on-demand and flexible programming of the CAH for liquid sampling.

## Methods

### Fabrication of the coplanar DC-electrowetting on dielectric (EWOD) chip.

ITO-coated glass were provided by Wesley Technology Co. Ltd. RZJ-304 photoresist and RZX-3038 developer were purchased from Suzhou Ruihong Electronic Chemical Co. Teflon® AF2400 was provided by DuPont. CEP was supplied by Shin-Etsu Chemical Co. Ltd. ITO etchant ITO-8200 was purchased from KunShan ChangYou Electronic Materials Co. Ltd.

The glass substrates were first cleaned sequentially with acetone, ethanol, and DI water and then dried with a nitrogen gun. The bottom electrodes were then patterned by photolithography and wet etching. First, RZJ-304 was spin-coated onto the substrate at 3000 rpm for 30 s, followed by soft-bake at 95 °C for 10 min. The coated substrate was then exposed for 3 s (15 mW/cm $^2$ ) through the electrode photomask and developed for 40 s in RZX-3038, rinsed in DI water, and hard-baked at 120 °C for 5 min. Finally, the ITO was etched in ITO-8200 for 30 s at 60 °C and thoroughly rinsed. The hard-baked photoresist was then stripped in acetone, and the substrate was rinsed with DI water and dried with a nitrogen gun.

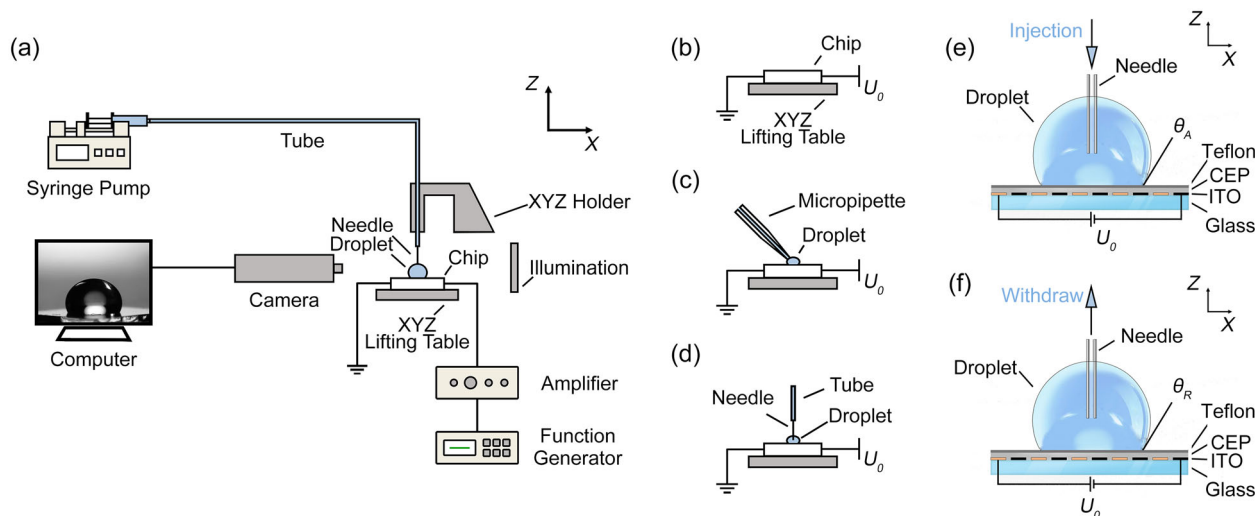


**Fig. 5 Experimental set-up and measurement process.** **a** Experimental set-up. **b–f** Apparent contact angle hysteresis measurement process. **b** The electrowetting on dielectric (EWOD) chip is charged by applying voltage  $U_0$  before adding a liquid sample, **c** droplet dispensing on the charged chip, **d** connection to the inlet tubing, **e** advancing contact angle ( $\theta_A$ ) measurement by adding liquid at constant voltage until the onset of contact line motion, **f** receding contact angle ( $\theta_R$ ) measurement by removing liquid at constant voltage. Abbreviations: ITO, indium tin oxide; CEP, cyanoethyl pullulan; XYZ, 3-axes translation stage.

The CEP powder was dissolved in *N,N*-dimethylformamide to produce a 15% (wt/wt) solution, which was then spin-coated onto the substrate at 3000 rpm for 30 s. After that, the CEP samples were annealed at 100 °C in atmosphere for an hour. This process was repeated twice to form a 408-nm-thick film.

Amorphous PTFE (AF2400) was dissolved in FC-40 at 1 wt% and then spin-coated at 3000 rpm on the substrate, followed by baking at 165 °C for 1 h, and left to rest at room temperature for 12 h approximately. This yields a 60-nm-thick PTFE layer. The substrates were used within 1 week after fabrication.

**Measurement of the CAH.** The coplanar electrowetting chip connected to a DC supply  $U_0$  was placed on the manipulation plate of a goniometer (DSA30, KRKRÜSS, Germany). The contact angles were then measured with the goniometer using side view images of the droplet. The liquid in the droplet was replenished or extracted via an inserted steel needle with the flow rate controlled by a syringe pump (5a).

The detailed process is as follows: A clean EWOD chip is loaded with a voltage  $U_0$  (Fig. 5b), then a droplet is deposited on the chip with a micropipette and spread by electrowetting until it reaches a stable shape (Fig. 5c). The needle connected to the syringe pump is then inserted into the droplet. The goniometer is very sturdy and no vibrations were observed. We then slowly vary the droplet volume by pumping liquid at a flow rate  $Q_1 = 1.0 \mu\text{L}/\text{min}$  while maintaining a constant voltage  $U_0$  (Fig. 5d). Advancing (receding) contact angles are measured at the onset of the contact line motion when injecting (withdrawing) liquid (Fig. 5e, f).

**Error bars.** The error bars in all graphs represent the standard error assuming a Gaussian distribution of the error, that is: standard error =  $\text{std}/\sqrt{n_{\text{exp}}}$ , with std the standard deviation and  $n_{\text{exp}}$  the number of experiment repeats.

**Model parameter estimation.** Equations (10b) and (10c) predict the CAH depending on the advancing and receding contact angles at  $U_0 = 0 \text{ V}$ , the areal capacitance  $C$ , the liquid–gas surface tension  $\gamma_{\text{lg}} = 71.97 \text{ mN}/\text{m}$  (for DI water<sup>64</sup>), the voltage  $U_0$ , and the electrode pitch-to-droplet radius ratio  $\frac{p}{R} \cos \theta_{A0} = -0.556$  and  $\cos \theta_{R0} = -0.510$  are input directly from experimental data.  $C \approx 0.350 \text{ mF}/\text{m}^2$  is obtained by fitting the evolution of mean contact angle depending on the voltage (see Supplementary Note 2). The droplet contact line radius  $R(U_0)$  is estimated by solving numerically the Young–Laplace equation (see Supplementary Note 4) with the contact angle  $\theta_E$  given by Eq. (11c).

## Data availability

The data that support the findings of this study are available from the authors upon reasonable request. The DOI of the data is <https://doi.org/10.6084/m9.figshare.14870877>.

Received: 5 November 2020; Accepted: 6 July 2021;

Published online: 26 August 2021

## References

- De Gennes, P. G. Wettings - statics and dynamics. *Rev. Mod. Phys.* **57**, 827 (1985).
- Eral, H. B., 't Mannetje, D. J. C. M. & Oh, J. M. Contact angle hysteresis: a review of fundamentals and applications. *Colloid Polym. Sci.* **291**, 247 (2013).
- Erbil, H. Y. The debate on the dependence of apparent contact angles on drop contact area or three-phase contact line: a review. *Surf. Sci. Rep.* **69**, 325 (2014).
- Johnson, R. E. J. & Dettre, R. H. In *Contact Angle, Wettability, and Adhesion, Advances in Chemistry* Ch. 7 (American Chemical Society, 1964).
- Cox, R. G. The spreading of a liquid on a rough solid surface. *J. Fluid Mech.* **131**, 1 (1983).
- Johnson, R. E. J. & Dettre, R. H. Contact angle hysteresis. III. Study of an idealized heterogeneous surface. *J. Phys. Chem.* **68**, 1744 (1964b).
- Priest, C., Sedev, R. & Ralston, J. Asymmetric wetting hysteresis on chemical defects. *Phys. Rev. Lett.* **99**, 026103 (2007).
- De Johge, V. & Chatain, D. Experimental study of wetting hysteresis on surfaces with controlled geometrical and/or chemical defects. *Acta Metall. Mater.* **43**, 1505 (1995).
- Leopoldes, J. & Bucknall, D. Droplet spreading on microstriped surfaces. *J. Phys. Chem. B* **109**, 8973 (2005).
- Good, R. J. A thermodynamic derivation of Wenzel's modification of Young's equation for contact angles - together with a theory of hysteresis. *J. Am. Chem. Soc.* **74**, 5041 (1952).
- Sun, Q. et al. Surface charge printing for programmed droplet transport. *Nat. Mater.* **18**, 936 (2019).
- Mugele, F. & Baret, J. C. Electrowetting: from basics to applications. *J. Phys. Condens. Matter* **17**, R705 (2005).
- Fair, R. B. Digital microfluidics: is a true lab-on-a-chip possible? *Microfluid. Nanofluid.* **3**, 245 (2007).
- Nelson, W. & Kim, C. J. Droplet actuation by electrowetting-on-dielectric (EWOD): a review. *J. Adhes. Sci. Technol.* **26**, 1747 (2012).
- Heikenfeld, J. et al. Electrofluidic displays using Young-Laplace transposition of brilliant pigment dispersions. *Nat. Photonics* **3**, 292 (2009).
- Hayes, R. A. & Feenstra, B. J. Video-speed electronic paper based on electrowetting. *Nature* **425**, 383 (2003).
- Li, C. & Jiang, H. Electrowetting-driven variable-focus microlens on flexible surfaces. *Appl. Phys. Lett.* **100**, 231105 (2012).
- Hao, C. et al. Electrowetting on liquid-infused film (EWOLF): complete reversibility and controlled droplet oscillation suppression for fast optical imaging. *Sci. Rep.* **4**, 6846 (2014).
- Heikenfeld, J. High-transmission electrowetting light valves. *Appl. Phys. Lett.* **86**, 151121 (2005).
- Murade, C. U., Oh, J. M., van den Ende, D. & Muggle, F. Electrowetting driven optical switch and tunable aperture. *Opt. Express* **19**, 15525 (2011).
- Lippmann, M. G. Relation entre les phenomenes electriques et capillaires. *Ann. Chim. Phys.* **5**, 494 (1875).

22. Jones, T. B. On the relationship of dielectrophoresis and electrowetting. *Langmuir* **18**, 4437 (2002).
23. Buehrle, J., Herminghaus, S. & Mugele, F. Interface profiles near three-phase contact lines in electric fields. *Phys. Rev. Lett.* **91**, 086101 (2003).
24. Bonn, D., Eggers, J., Indekeu, J., Meunier, J. & Rolley, E. Wetting and spreading. *Rev. Mod. Phys.* **81**, 739 (2009).
25. Mugele, F. & Buehrle, J. Equilibrium drop surface profiles in electric fields. *J. Phys. Condens. Matter* **19**, 375112 (2007).
26. Israelachvili, J. N. (ed.) In *Intermolecular and Surface Forces* 3rd edn Ch 17.1 (Academic Press, 2011).
27. 't Mannetje, D. et al. Electrically tunable wetting defects characterized by a simple capillary force sensor. *Langmuir* **29**, 9944 (2013).
28. 't Mannetje, D. et al. Trapping of drops by wetting defects. *Nat. Commun.* **5**, 4559 (2014).
29. Nelson, W. C., Sen, P. & Kim, C. J. Dynamic contact angles and hysteresis under electrowetting-on-dielectric. *Langmuir* **27**, 10319 (2011).
30. McHale, G., Brown, C. V., Newton, M. I., Wells, G. G. & Sampara, N. Dielectrowetting driven spreading of droplets. *Phys. Rev. Lett.* **107**, 186101 (2011).
31. Bhushan, B. & Pan, Y. Role of electric field on surface wetting of polystyrene surface. *Langmuir* **27**, 9425 (2011).
32. Li, F. & Mugele, F. How to make sticky surfaces slippery: contact angle hysteresis in electrowetting with alternating voltage. *Appl. Phys. Lett.* **92**, 244108 (2008).
33. Nita, S. et al. Electrostatic cloaking of surface structure for dynamic wetting. *Sci. Adv.* **3**, e1602202 (2017).
34. Yi, U. C. & Kim, C. J. Characterization of electrowetting actuation on addressable single-side coplanar electrodes. *J. Micromech. Microeng.* **16**, 2053 (2006).
35. Wang, Y. & Bhushan, B. Liquid microdroplet sliding on hydrophobic surfaces in the presence of an electric field. *Langmuir* **26**, 4013 (2009).
36. Manukyan, G., Oh, J. M., van den Ende, D., Lammertink, R. G. H. & Mugele, F. Electrical switching of wetting states on superhydrophobic surfaces: a route towards reversible Cassie-to-Wenzel transitions. *Phys. Rev. Lett.* **106**, 014501 (2011).
37. Gao, J., Mendel, N., Dey, R., Baratian, D. & Mugele, F. Contact angle hysteresis and oil film lubrication in electrowetting with two immiscible liquids. *Appl. Phys. Lett.* **112**, 203703 (2018).
38. Zhao, R., Liu, Q. C., Wang, P. & Liang, Z. C. *Chin. Phys. B* **24**, 086801 (2015).
39. Joanny, J. F. & De Gennes, P. G. A model for contact angle hysteresis. *J. Chem. Phys.* **81**, 552 (1984).
40. Yuan, Q. & Zhao, Y. P. Precursor film in dynamic wetting, electrowetting, and electro-elasto-capillarity. *Phys. Rev. Lett.* **104**, 246101 (2010).
41. Huh, C. & Mason, S. G. Effects of surface roughness on wetting (theoretical). *J. Colloid Interf. Sci.* **60**, 11 (1977).
42. Wang, W. et al. On-demand contact line pinning during droplet evaporation. *Sens. Actuators B* **312**, 127983 (2020).
43. Choi, W., Tuteja, A., Mabry, J. M., Cohen, R. E. & McKinley, G. H. A modified Cassie-Baxter relationship to explain contact angle hysteresis and anisotropy on non-wetting textured surfaces. *J. Colloid Interface Sci.* **339**, 208 (2009).
44. Chen, J. et al. Study of cyanoethyl pullulan as insulator for electrowetting. *Sens. Actuators B* **199**, 183 (2014).
45. Yatsuzuka, K., Mizuno, Y. & Asano, K. Electrification phenomena of pure water droplets dripping and sliding on a polymer surface. *J. Electroanal. Chem.* **32**, 157 (1994).
46. Stetten, A. Z., Golovko, D. S., Weber, S. A. L. & Butt, H.-J. Slide electrification: charging of surfaces by moving water drops. *Soft Matter* **15**, 8667 (2019).
47. Wu, H. et al. Electrically controlled localized charge trapping at amorphous fluoropolymer-electrolyte interfaces. *Small* **16**, 1905726 (2020).
48. Mugele, F. & Herminghaus, S. Electrostatic stabilization of fluid microstructures. *Appl. Phys. Lett.* **81**, 2302 (2002).
49. Liu, J., Wang, M., Chen, S. & Robbins, M. O. Uncovering molecular mechanisms of electrowetting and saturation with simulations. *Phys. Rev. Lett.* **108**, 216101 (2012).
50. Klarman, D., Andelman, D. & Urbakh, M. A model of electrowetting, reversed electrowetting, and contact angle saturation. *Langmuir* **27**, 6031 (2011).
51. Chevalliot, S., Kuiper, S. & Heikenfeld, J. Experimental validation of the invariance of electrowetting contact angle saturation. *J. Adhes. Sci. Technol.* **26**, 1909 (2012).
52. Papanasiou, A. G., Papaioannou, A. T. & Boudouvis, A. G. Illuminating the connection between contact angle saturation and dielectric breakdown in electrowetting through leakage current measurements. *J. Appl. Phys.* **103**, 034901 (2008).
53. Peykov, V., Quinn, A. & Ralston, J. Electrowetting: a model for contact-angle saturation. *Colloid Polym. Sci.* **278**, 789 (2000).
54. Jansen, H. P., Bliznyuk, O., Kooij, E. S., Poelsema, B. & Zandvliet, H. J. Simulating anisotropic droplet shapes on chemically striped patterned surfaces. *Langmuir* **28**, 499 (2012).
55. Bliznyuk, O., Vereshchagina, E., Kooij, E. S. & Poelsema, B. Scaling of anisotropic droplet shapes on chemically stripe-patterned surfaces. *Phys. Rev. E* **79**, 041601 (2009).
56. Damlé, V. G. & Rykaczewski, K. Nano-striped chemically anisotropic surfaces have near isotropic wettability. *Appl. Phys. Lett.* **110**, 171603 (2017).
57. Banpurkar, A. G., Nichols, K. P. & Mugele, F. Electrowetting-based microdrop tensiometer. *Langmuir* **24**, 10549 (2008).
58. De Gennes, P.-G., Brochard-Wyart, F. & Quéré, D. *Capillarity and Wetting Phenomena: Drops, Bubbles, Pearls, Waves*, Vol. 57 (Springer Science, Business Media, 2013).
59. Mugele, F. Fundamental challenges in electrowetting: from equilibrium shapes to contact angle saturation and drop dynamics. *Soft Matter* **5**, 3377 (2009).
60. Roura, P. & Fort, J. Local thermodynamic derivation of Young's equation. *J. Colloid Interface Sci.* **272**, 420 (2004).
61. Morgan, H., Izquierdo, A. G., Bakewell, D., Green, N. G. & Ramos, A. The dielectrophoretic and travelling wave forces generated by interdigitated electrode arrays: analytical solution using Fourier series. *J. Phys. D Appl. Phys.* **34**, 1553 (2001).
62. Gunda, N. S. K. & Mitra, S. K. Modeling of dielectrophoretic transport of myoglobin molecules in microchannels. *Biomicrofluidics* **4**, 014105 (2010).
63. Vo, Q., Fujita, Y., Tagawa, Y. & Tran, T. Anisotropic behaviours of droplets impacting on dielectrowetting substrates. *Soft Matter* **16**, 2621 (2020).
64. Coker, A. K. *Fortran Programs for Chemical Process Design, Analysis, and Simulation* (Elsevier, 1995).

### Acknowledgements

We are indebted to Kaidi Zhang for the fabrication of the first batch of EWOD devices. This work was supported by the National Natural Science Foundation of China with Grant Nos. 12004078, 51950410582, 61874033, and 61674043, the Science Foundation of Shanghai Municipal Government with Grant Nos. 18ZR1402600, and the State Key Lab of ASIC and System, Fudan University with Grant No. 2018MS003, 2020KF006, 2021MS001, 2021KF003 and 2021MS002. This work was supported by the Fundamental Research Funds for the Central Universities with Grant No. D5000210626.

### Author contributions

W.W., J.Z. and A.R. designed the research; W.W. and Q.W. conducted the experiments; W.W. and A.R. interpreted the results and derived the model; W.W., Q.W., J.Z. and A.R. wrote the manuscript.

### Competing interests

The authors declare no competing interests.

### Additional information

**Supplementary information** The online version contains supplementary material available at <https://doi.org/10.1038/s42005-021-00691-4>.

**Correspondence** and requests for materials should be addressed to J.Z. or A.R.

**Peer review information** *Communications Physics* thanks Amy Stetten and the other anonymous reviewer(s) for their contribution to the peer review of this work. Peer reviewer reports are available.

**Reprints and permission information** is available at <http://www.nature.com/reprints>

**Publisher's note** Springer Nature remains neutral with regard to jurisdictional claims in published maps and institutional affiliations.



**Open Access** This article is licensed under a Creative Commons Attribution 4.0 International License, which permits use, sharing, adaptation, distribution and reproduction in any medium or format, as long as you give appropriate credit to the original author(s) and the source, provide a link to the Creative Commons license, and indicate if changes were made. The images or other third party material in this article are included in the article's Creative Commons license, unless indicated otherwise in a credit line to the material. If material is not included in the article's Creative Commons license and your intended use is not permitted by statutory regulation or exceeds the permitted use, you will need to obtain permission directly from the copyright holder. To view a copy of this license, visit <http://creativecommons.org/licenses/by/4.0/>.

© The Author(s) 2021